Supplementary Geological and Petrographic Information

The Betic Cordillera (southern Spain) represents the westernmost part of the peri-Mediterranean Alpine orogen formed during the convergence of Africa and Eurasia from Late Cretaceous to Tertiary times. During this orogenic process, large bodies of subcontinental lithospheric mantle (the Ronda Peridotites; Obata, 1980) were emplaced within the metasedimentary continental crust, in the Internal Zone of Betic Cordillera. The emplacement of mantle rocks produced high-temperature metamorphism and partial melting in the adjacent crustal rocks (Tubia and Cuevas, 1986; Tubia et al., 1997; Platt and Whitehouse, 1999; Acosta-Vigil et al., 2001). In the dynamothermal aureole located below the Ronda peridotites, the intensity of the deformation and the degree of melting increase towards the contact with the mantle rocks and the migmatites range from metatexites, through diatexites, to mylonitic diatexites (Acosta-Vigil et al., 2001). The mylonitic migmatites at the contact with the peridotites show metamorphic peak conditions of ~800 °C and ~8 kbar (Tubia et al., 1997).

The selected migmatite (ALP1) was collected at Sierra Alpujata (N 36°36′37.6″, W 4°49′15.6″), ~400 m below the contact with the peridotite (Fig. DR1). It is a stromatic metatexite with thin (< 1 cm) leucosomes sub-parallel to the foliation defined by biotite and fibrolitic sillimanite (see also Figs. 1b and 2b in Ferrero et al., 2012). The stable mineral assemblage is composed of quartz, plagioclase, K-feldspar, biotite, fibrolite, garnet and graphite. Rare muscovite is included in K-feldspar crystals or associated with biotite and sillimanite in the rock matrix. Leucosomes contain quartz, plagioclase, K-feldspar and biotite. Garnet occurs in the neosome as small idioblastic porphyroblasts (80-200 μm in diameter) in very low modal amount (< 1%, determined by thermodynamic modeling) and contains clusters of several primary melt inclusions (Fig. 1B; see also Fig. 1a in Cesare et al., 2011 and Fig. 1f in Ferrero et al., 2012). The *P-T* conditions of melting in the studied metatexite were constrained using two pseudosections in the MnNCKFMASHTO system (Tajcmanova et al., 2011; Bartoli et al., in preparation): one was constructed for the bulk rock and the other for the composition of re-homogenized *nanogranite* inclusion. In the former, compositional isopleths for chemical parameters of garnet and biotite constrain the conditions of equilibration in the range 680-750 °C and 3.5-5.5 kbar. Combining these constraints with the melt field obtained in the pseudosection for the *nanogranite* provides 680-700 °C and 4.5-4.8 kbar as conditions for the onset of melting in the studied metatexite. The complete re-homogenization of *nanogranite* inclusions without garnet dissolution at 700 °C (see main text) is a strong constraint and indicates that garnet grew and trapped melt inclusions at this temperature, or even at slightly lower values. The crystallization of small amounts (< 1%) of peritectic garnet at temperatures that would be in general considered too low for its occurrence, can be explained by the combined effects of the breakdown of Fe-bearing muscovite (up to ~2

wt% of FeO, Tab. DR3) and of a continuous reaction involving biotite melting (Tajcmanova et al., 2011; Bartoli et al., in preparation).

Supplementary Methods:

Garnet separation: single garnet crystals were obtained by initial crushing of the rock followed by steps through an agate mortar mill. The powder was sieved and the crystals with grain-size between 50 and 200 μm were passed through the Frantz isodynamic magnetic separator at Dipartimento di Scienze della Terra, Università di Parma (Italy). A 100% pure concentrate was obtained by hand-picking under a binocular microscope.

Experimental re-homogenization of melt inclusions: piston cylinder experiments were performed at Laboratory of Experimental Petrology, Dipartimento di Scienze della Terra, Università di Milano (Italy). After garnet separation, single garnet crystals were loaded into Au capsules (Ø=3 mm) alternating them with powdered silica. Bi-distilled water (~10 wt %) was added in some capsules to evaluate the potential effects of H_2O diffusion out of the MI during experiments. The capsules were crimped and sealed by arc welding using a wet tissue around the capsule to prevent H_2O loss. No weight loss of capsules with added H_2O was observed after repeated heating at ~100°C. For each run 2 dry and 1 wet capsules were embedded in MgO-salt, and a low friction assembly consisting of NaCl sleeve and graphite heater was used. The experiments were run at 5 kbar, 700, 750 and 800°C for 24 h. The temperature was controlled by K-type thermocouples and was considered accurate to ±5°C. Pressure was measured by a load cell into the frame (Johannes-type piston cylinder) and accurate to ±0.4 kbar. At the end of the experiments, the capsules were quenched and mounted in epoxy and the inclusions in the garnet were exposed by polishing. An aqueous fluid bubbling out of the capsules with added H_2O was observed during capsule opening.

Scanning electron microscopy: backscattered electron (BSE) images of melt inclusions were obtained using a Jeol JSM-6500F thermal Field Emission Scanning Electron Microscope (FESEM) available at the High Temperature/High Pressure Laboratory, Istituto Nazionale di Geofisica e Vulcanologia (I.N.G.V.), Rome (Italy).

Electron microprobe: chemical composition of glass in re-homogenized melt inclusions at 700 °C and 5 kbar was obtained using a Jeol JXA 8200 Superprobe equipped with 5 spectrometers at the Dipartimento di Scienze della Terra, Università di Milano (Italy). Analytical parameters were: 15 kV accelerating voltage, 2 nA current, 1 μm beam diameter and a counting time of 10 s on peak and 2 s on background. Na, K, Al and Si were analyzed first. Natural silicates were used as standards. Owing to Na loss during electron microprobe analysis of rhyolitic glasses with consequences also on K, Al and Si amounts (Morgan and London, 1996, 2005), their concentrations were corrected using conservative factors obtained by the analysis of

leucogranitic glasses of known composition (ASI=1.01-1.02) with H_2O contents as close as possible to the analyzed samples (from 4.3 to 10.1 wt% H_2O), at the same working conditions. This procedure should provide reasonable results (Morgan and London, 2005).

The compositions of muscovite, biotite and feldspars were obtained using a Jeol JXA 8200 Superprobe at the Dipartimento di Scienze della Terra, Università di Milano (Italy). Analytical parameters were: 15 kV accelerating voltage, 5 nA current, counting time of 30 s on peak and 10 s on background. Garnet compositions were determined using the Cameca SX50 microprobe of the C.N.R.-I.G.G. (Consiglio Nazionale delle Ricerche-Istituto di Geoscienze e Georisorse), at the Dipartimento di Geoscienze, Università di Padova, Italy. Measurements were performed using 20 kV accelerating voltage, 20 nA beam current, counting time of 10 s on peak and 5 s on background. Natural and synthetic silicates and oxides were used as standards.

X-ray fluorescence: bulk rock analyses of major elements were performed employing a Pan-Alytical XRF Spectrometer PW2400 at the Dipartimento di Geoscienze, Università di Padova (Italy).

Raman spectroscopy: Raman spectroscopy was performed to determine H_2O contents of the glassy MI exposed on the garnet surface, following the method proposed by Thomas (2000), which is based on the linear relationship between the H_2O content of rhyolitic glass and the intensity of the asymmetric OH stretching band at 3550 cm^{-1}. No significant differences were observed for MI that were analyzed by Raman both before and after being exposed at the surface (Severs et al., 2007). After a detailed optical investigation to verify the homogeneity of MI, their H_2O content was determined using a Jobin Yvon Horiba HR 800 Labram confocal Raman microprobe equipped with an Olympus BX 41 petrographic microscope, at the Fluids Research Laboratory, Department of Geosciences, Virginia Tech (USA). The excitation source was a 514.57 nm (green) Laser Physics 100S-514 Ar$^+$ laser. The analytical settings were a 150 μm slit width, 400 μm confocal aperture, 600 grooves/mm gratings, 100x objective, 3x accumulations and 100 s acquisition time. Spectra were collected between 2600 cm^{-1} and 4000 cm^{-1}. The area under the 3550 cm^{-1} peak was determined after baseline correction. The calibration procedures were performed using 5 synthetic glasses with known H_2O contents, ranging between 2.17 and 10.11 wt%. Four of the standards (Ab1196A, 040281I, 032481VII and 022881XII; Severs et al., 2007) have compositions in the $(Na,K)AlSi_3O_8$ system and the fifth (LGB; Behrens and Jantos, 2001) has a leucogranitic composition. The intensity of the Raman peak is directly proportional to H_2O concentration and is confirmed to be independent of the composition of the glass, as documented by Thomas (2000). The data fit on straight lines (Fig. DR3) indicating the linear relationship between the H_2O content in glass and the area under the asymmetric OH stretch band at 3550 cm^{-1}. After each MI analysis the Raman calibration was verified using one of synthetic glasses described above and the H_2O content of MI was determined by comparison of H_2O peak area for the single standard and the melt inclusion. The ratio between the H_2O peak

area for the standard and that for the melt inclusion equals the ratio of the H_2O content of the standard and melt inclusion (see also Thomas et al., 2006 and Severs et al., 2007). Repeated analyses of the same spot on some MI yielded standard deviation between ±0.1 and ±0.3 wt% H_2O. There is no correlation between H_2O content and inclusion size.

Bubbles in MI remelted at 750 and 800 °C were analyzed using the same Raman instrument described above. The analytical settings for these analyses were a 150 μm slit width, 400 μm confocal aperture, 600 grooves/mm gratings, 100x objective, 3x accumulations and 30 s acquisition time. Spectra were collected between 100 cm^{-1} and 4000 cm^{-1}. CO_2 density was determined from the Raman spectra according to the method based on the dependence of the CO_2 Fermi diad splitting from density (Fall et al., 2011). The position of Raman lines was determined after baseline correction.

Raman hyperspectral images of liquid-H_2O distribution in crystallized MI were obtained with a Labram Raman instrument (Horiba, Jobin-Yvon), equipped with a Peltier-cooled CCD detector and a polarized 514.5 nm Ar^+ laser at the Dipartimento di Scienze della Terra, Università di Siena (Italy). The laser power was 300 mW at the source, and the slit width was 200 μm, with a spectral resolution of 1.5 cm^{-1}. Raman spectra were collected through an excitation spot of 1x1x5 μm in volume (100x objective, n.a.=0.9). Acquisition time was 40 s. Hyperspectral images were collected following a regular grid of points equidistant 1 μm in both directions, using a computer-controlled, automated X-Y mapping stage (Horiba, Jobin Yvon).

Table DR1: Raman results of CO_2 density at room temperature in bubbles from melt inclusions remelted at 750°C and 5 kbar.

No. analyses	4
v+ (cm^{-1})	1389.47 (0.78)
v- (cm^{-1})	1286.46 (0.79)
Δ (cm^{-1})	103.01 (0.00)
ρ (g/cm^3)	0.14 (0.00)

v+ and v- represent the upper and lower bands
respectively of Fermi diad. Δ: difference between the
positions of the v+ and v- bands. ρ: density of CO_2.
Numbers in parentheses refer to 1σ standard deviations.

Table DR2: Chemical compositions of re-homogenized melt inclusions at 700 °C and 5 kbar (MI) and leucosomes (LS) from metatexite ALP1. Viscosities of the leucogranitic melts trapped in MI are also shown.

	MI	MI	LS	LS	LS
Exp. conditions	dry	wet			
No. analyses	15	13			
SiO$_2$	70.03 (2.36)	69.60 (1.86)	73.56	72.49	80.92
TiO$_2$	0.04 (0.07)	0.06 (0.07)	0.16	0.15	0.09
Al$_2$O$_3$	11.71 (0.89)	12.06 (0.49)	14.54	14.71	10.2
Fe$_2$O$_3$*			1.04	1.03	0.64
FeO†	1.71 (0.22)	1.74 (0.25)			
MnO	0.17 (0.10)	0.16 (0.10)	0.02	0.02	0.02
MgO	0.12 (0.07)	0.12 (0.07)	0.27	0.26	0.18
CaO	0.45 (0.13)	0.45 (0.10)	1.02	0.93	1.01
Na$_2$O	2.79 (0.37)	2.85 (0.50)	2.33	2.28	1.96
K$_2$O	4.05 (0.41)	4.08 (0.30)	6.13	6.76	4.15
P$_2$O$_5$	0.26 (0.24)	0.22 (0.14)	0.14	0.14	0.11
LOI			0.48	0.53	0.36
Total	91.33 (2.26)	91.34 (2.12)	99.69	99.31	99.64
H$_2$O §	5.1 (1.30)	5.0 (1.46)			
ASI	1.20 (0.08)	1.22 (0.10)	1.18	1.15	1.07
#Mg	0.10 (0.06)	0.10 (0.05)	0.50	0.50	0.53
CIPW norm					
Qtz	36.12 (3.70)	35.31 (2.62)	34.37	31.36	51.48
Crn	2.36 (0.91)	2.64 (1.08)	2.56	2.28	0.91
Or	23.95 (2.40)	24.14 (1.77)	36.23	39.97	24.55
Ab	23.64 (3.09)	24.11 (4.19)	19.70	19.27	16.61
An	0.99 (1.20)	0.84 (0.58)	4.13	3.73	4.28
log η (Pa s) **	5.95 (0.66)	6.00 (0.75)			
log η (Pa s) ††	5.76 (0.87)	5.79 (0.98)			

Major and minor elements and H$_2$O are in wt%. Numbers in parentheses refer to 1σ standard deviations

*Total Fe as Fe$_2$O$_3$

†Total Fe as FeO

LOI: loss on ignition

§H$_2$O determined by Raman spectroscopy

ASI = mol. Al$_2$O$_3$/(CaO+Na$_2$O+K$_2$O)

#Mg = mol. MgO/(MgO+FeO$_{tot}$)

**Viscosity calculated from Giordano et al. (2008), considering a temperature of 700 °C

††Viscosity calculated from Scaillet et al. (1996), considering a temperature of 700 °C

Table DR3: Representative electron microprobe analyses of the analyzed minerals from metatexite ALP1.

|	Ms	Ms	Bt	Bt	Grt	Grt	Pl	Pl	Kfs	Kfs
Na_2O	0.53	0.47	0.21	0.15	0.05	0.00	7.57	7.70	2.23	1.91
MgO	0.82	0.65	6.47	6.38	2.61	3.18	0.01	0.01	0.01	0.00
Al_2O_3	35.06	35.28	19.96	19.88	21.64	21.16	25.40	25.13	18.65	18.94
SiO_2	46.26	47.36	35.26	34.89	37.48	36.83	59.74	59.98	65.63	64.89
K_2O	10.41	10.34	9.26	9.51			0.32	0.26	13.41	13.86
CaO	0.01	0.01	0.04	0.01	0.96	0.91	6.79	6.50	0.07	0.10
TiO_2	0.29	0.18	4.22	4.29	0.04	0.00	0.05	0.03	0.04	0.01
Cr_2O_3	0.04	0.00	0.11	0.03						
MnO	0.01	0.00	0.21	0.18	3.96	3.29	0.02	0.09	0.00	0.02
FeO	1.84	1.22	22.16	21.68	34.92	35.14	0.06	0.00	0.01	0.02
BaO	0.04	0.03	0.03	0.02						
F	0.00	0.00	0.39	0.28						
Cl	0.01	0.02	0.07	0.07						
Tot.	95.33	95.56	98.39	97.37	101.66	100.50	99.96	99.70	100.05	99.75
O=F,Cl	0.00	0.00	-0.18	-0.13						
Tot.	95.33	95.55	98.21	97.24						
		22 (O)			12 (O)			8 (O)		
Si	6.170	6.260	5.260	5.259	2.983	2.967	2.665	2.679	2.998	2.981
Ti	0.029	0.018	0.474	0.486	0.003	0.000	0.002	0.001	0.001	0.000
Al	5.511	5.496	3.509	3.532	2.029	2.009	1.335	1.323	1.004	1.026
Cr	0.004	0.000	0.013	0.003						
Fe^{2+}	0.205	0.135	2.764	2.733	2.324	2.367	0.002	0.000	0.000	0.001
Mn	0.002	0.000	0.027	0.023	0.267	0.224	0.001	0.003	0.000	0.001
Mg	0.164	0.129	1.439	1.434	0.310	0.381	0.000	0.000	0.001	0.000
Ca	0.001	0.002	0.006	0.002	0.082	0.078	0.325	0.311	0.003	0.005
Na	0.138	0.120	0.062	0.044	0.007	0.000	0.655	0.667	0.198	0.170
K	1.771	1.744	1.762	1.829			0.018	0.015	0.782	0.812
Ba	0.002	0.001	0.002	0.001						
F	0.000	0.000	0.184	0.034						
Cl	0.002	0.004	0.018	0.017						
X_{Mg}			0.34	0.34	0.12	0.14				
Alm					0.78	0.78				
Prp					0.10	0.12				
Sps					0.09	0.07				
Grs					0.03	0.03				
Ab							0.66	0.67	0.20	0.17
An							0.33	0.31	0.00	0.01
Or							0.01	0.02	0.80	0.82
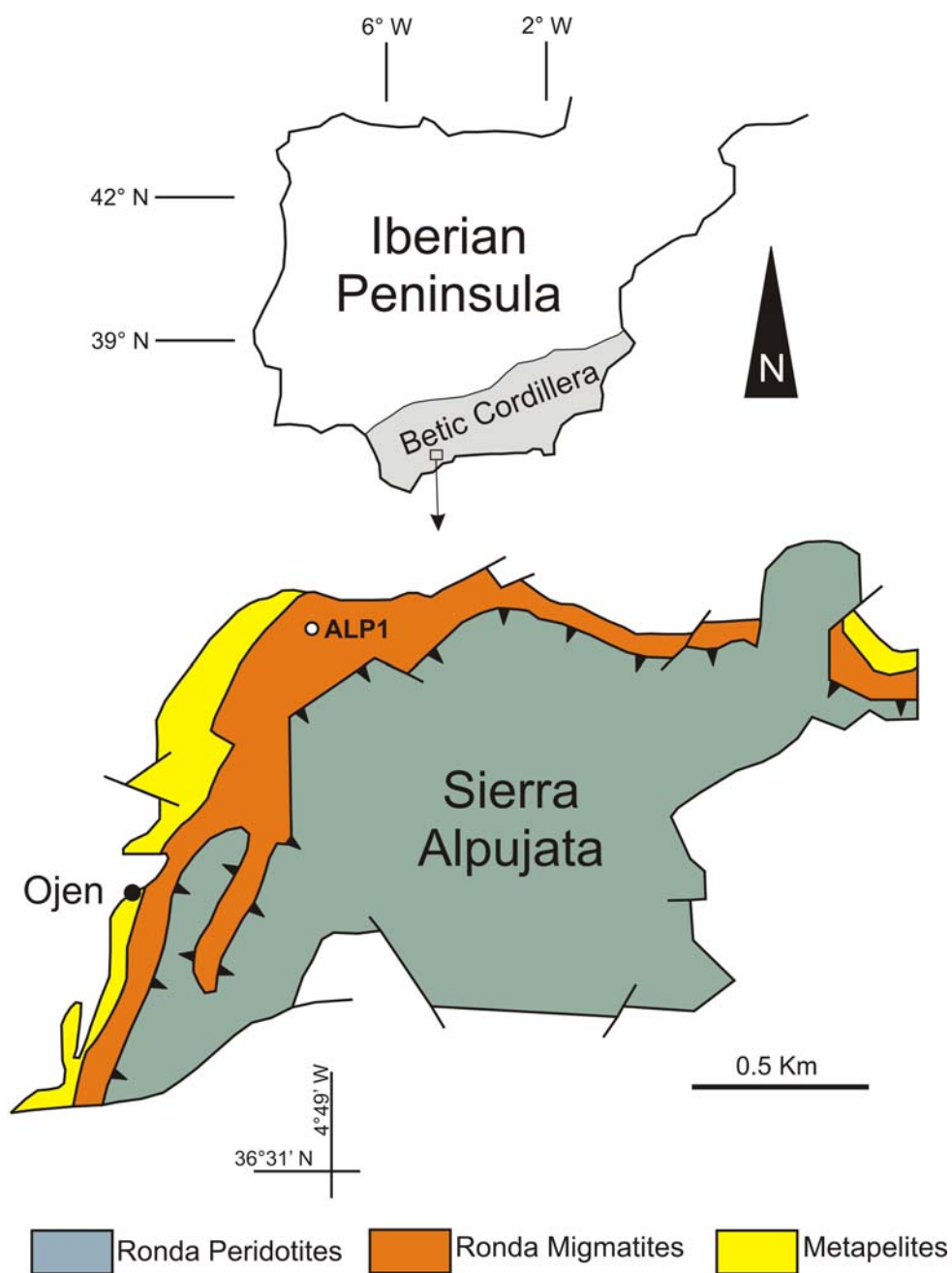
Figure DR1: Geological map of the Sierra Alpujata massif, showing the location of the studied metatexite (ALP1). Modified from Esteban et al., 2011.
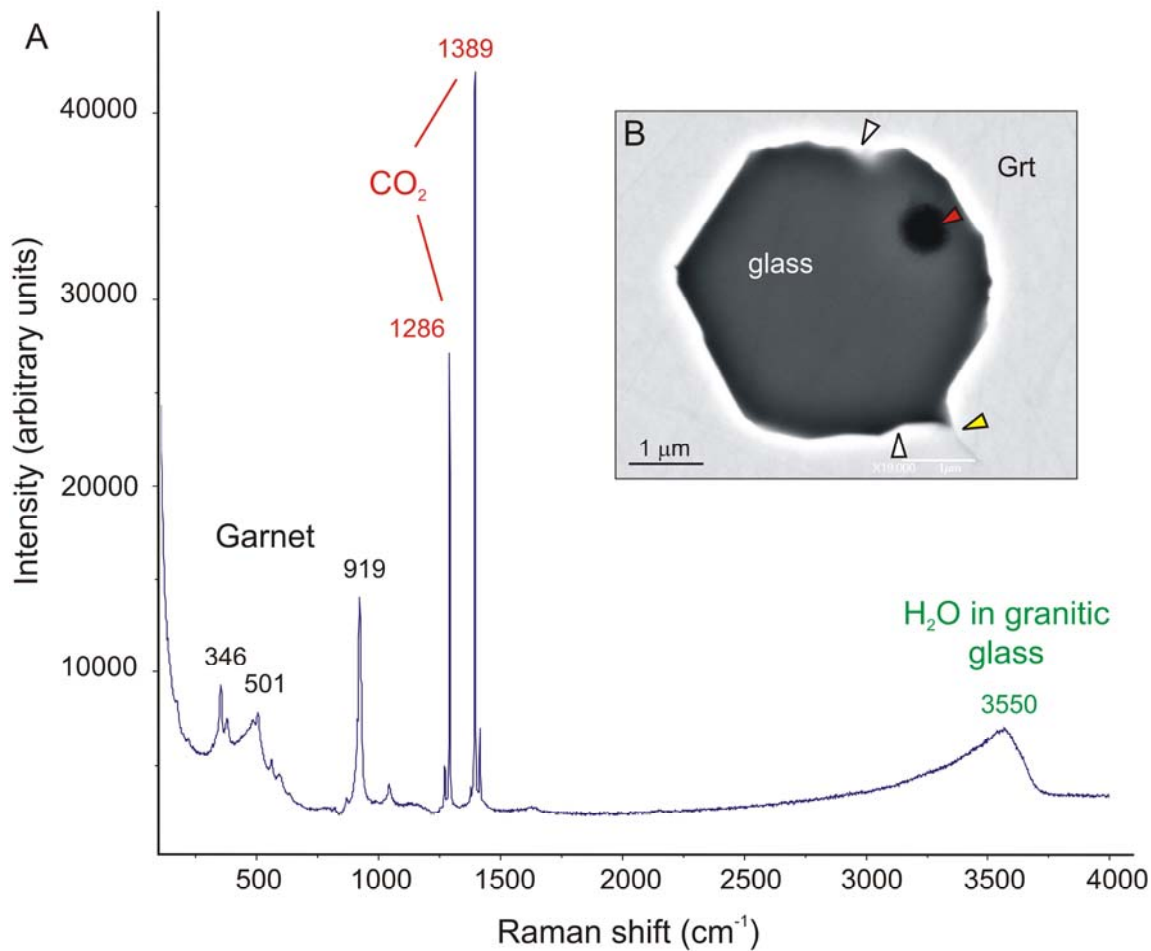
Figure DR2: A: Representative Raman spectrum of a CO_2 bubble within a re-melted melt inclusions, preserved below the inclusion surface. The asymmetric OH stretching band centered at 3550 cm^{-1} indicates that H_2O is present into the glass. B: FESEM BSE image of a melt inclusion re-melted at 800°C and 5 kbar that contain a CO_2 bubble (red arrow). After the experimental runs at 800 and 750 °C, re-melted inclusions generally show irregular boundaries (whire arrows) and decrepitation cracks (yellow arrow), suggesting that the trapping temperature was exceeded.
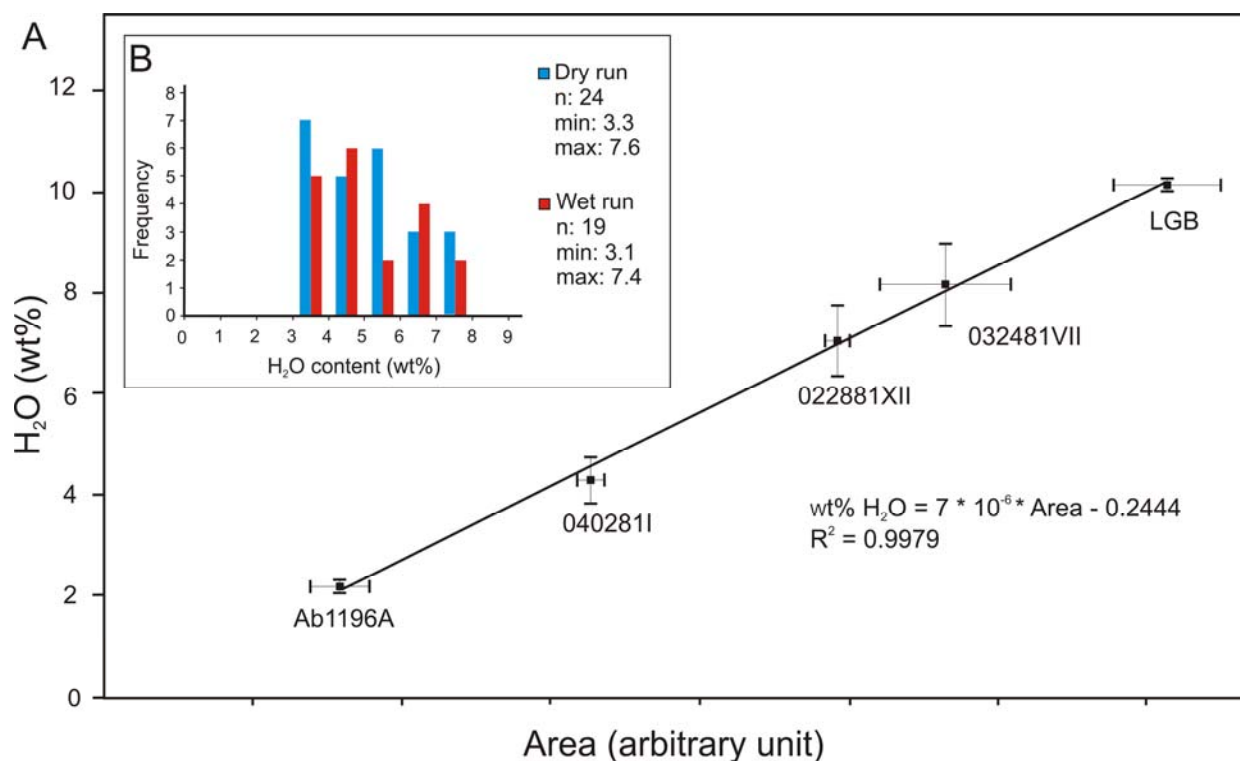
Figure DR3: H_2O quantification in silicate glasses using Raman spectroscopy. A: Raman calibration curve showing the linear relationship between the H_2O content of synthetic hydrous glasses with known water content and the area under the 3550 cm^{-1} peak (correlation coefficient $R^2 = 0.9979$). Horizontal bars indicate the standard deviation (1σ) after 3 replicated analyses across the reference glass. Vertical bars represent the analytical errors on H_2O quantification in the standard glasses from literature (Behrens and Jantos, 2001; Severs et al., 2007). B: Histogram of the H_2O content (wt%) from 43 glassy melt inclusions re-homogenized in dry and wet experiments at 700 °C and 5 kbar. The H_2O concentration for each MI was calculated from the geometric proportion between the H_2O peak area of a reference glass and that of melt inclusion measured under the same conditions (Thomas et al., 2006).
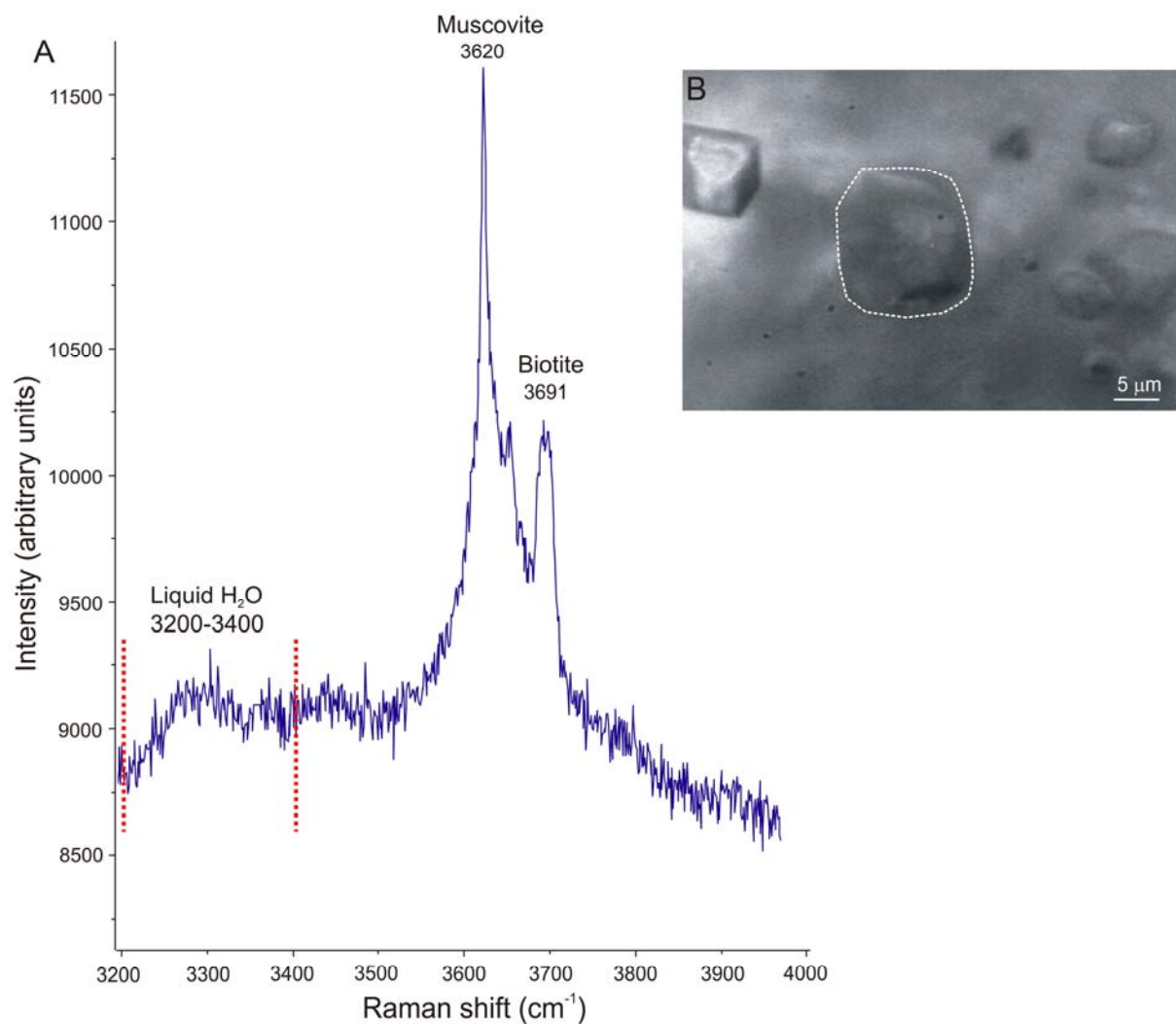
Figure DR4: Raman mapping of liquid H_2O distribution within a crystallized melt inclusion (*nanogranite*). A: Representative Raman spectrum obtained from mapping: the peaks at 3620 and 3691 cm^{-1} correspond to main OH stretching vibrations in muscovite and biotite, respectively. B: Investigated inclusion below garnet surface, PPL. The inclusion contains both hydroxylated minerals and free H_2O in the pores (see Fig. 4).

REFERENCES

Acosta-Vigil, A., Pereira, M.D., Shaw, D.M., and London, D., 2001, Contrasting behavior of boron during crustal anatexis: Lithos, v. 56, p. 15-31.

Behrens, H., and Jantos, N., 2001, The effect of anhydrous composition on water solubility in granitic melts: American Mineralogist, v. 86, p. 14-20.

Cesare, B., Acosta-Vigil, A., Ferrero, S., and Bartoli, O., 2011, Melt inclusions in migmatites and granulites, *in* Forster, M.A., and Fitz Gerald, J.D., eds., The Science of Microstructure - Part II, Journal of the Virtual Explorer, Electronic Edition, ISSN 1441-8142, v. 38, paper 2.

Esteban, J.J., Tubia, J.M., Cuevas, J., Vegas, N., Sergeev, S., and Larionov, A., 2011, Peri-Gondwanan provenance of pre-Triassic metamorphic sequences in the western Alpujarride nappes (Betic Cordillera, southern Spain): Gondwana Research, v. 20, p. 443-449.

Fall, A., Tattitch, B., and Bodnar, R.J., 2011, Combined microthermometric and Raman spectroscopic technique to determine the salinity of H_2O-CO_2-NaCl fluid inclusions based on clathrate melting: Geochimica and Cosmochimica Acta, v. 75, p. 951-964.

Ferrero, S., Bartoli, O., Cesare, B., Salvioli-Mariani, E., Acosta-Vigil, A., Cavallo, A., Groppo, C., and Battiston, S., 2012, Microstructures of melt inclusions in anatectic metasedimentary rocks: Journal of Metamorphic Geology, v. 30, p. 303-322.

Giordano, D., Russell, J.K., and Dingwell, D.B., 2008, Viscosity of magmatic liquids: A model: Earth and Planetary Science Letters, v. 271, p. 123–134.

Morgan, G.B. & London, D., 1996. Optimizing the electron microprobe analysis of hydrous alkali aluminosilicate glasses: American Mineralogist, v. 81, p. 1176–1185.

Morgan, G.B., IV and London, D., 2005, Effect of current density on the electron microprobe analysis of alkali aluminosilicate glasses: American Mineralogist, v. 90, p. 1131-1138.

Obata, M., 1980, The Ronda peridotite: garnet-, spinel-, and plagioclase-lherzolite facies and the P-T trajectories of a high temperature mantle intrusion: Journal of Petrology, v. 21, p. 533-572 .

Platt, J.P., and Whitehouse, M.J., 1999, Early Miocene high-temperature metamorphism and rapid exhumation in the Betic Cordillera (Spain): Evidence from U-Pb zircon ages: Earth and Planetary Science Letters, v. 171, p. 591-605.

Scaillet, B., Holtz, F., Pichavant, M., and Schmidt, M., 1996, Viscosity of Himalayan leucogranites: Implications for mechanisms of granitic magma ascent: Journal of Geophysical Research, v. 101, no. B12, p. 27691–27699.

Severs, M.J., Azbej, T., Thomas, J.B., Mandeville, J.B., and Bodnar, R.J., 2007, Experimental determination of H_2O loss from melt inclusions during laboratory heating: evidence from Raman spectroscopy: Chemical Geology, v. 237, p. 358-371.

Tajcmanova, L., Bartoli, O., Cesare, B., and Acosta-Vigil, A., 2011, Constraining the P-T conditions of melting in stromatic migmatites from Ronda (S Spain): Mineralogical Magazine, v. 75, no. 3, p. 1982.

Thomas, R., 2000, Determination of water contents of granite melt inlusions by confocal laser Raman microprobe spectroscopy: American Mineralogist, v. 85, p. 868-872.

Thomas, R., Kamenetsky, V. S., and Davidson P., 2006, Laser Raman spectroscopic measurements of water in unexposed glass inclusions: American Mineralogist, v. 91, p.467-470.

Tubía, J.M., and Cuevas, J. , 1986, High-temperature emplacement of the Los Reales peridotite nappe (Betic Cordillera, Spain): Journal of. Structural Geology, v. 8, p. 473-482.

Tubía, J.M., Cuevas, J., and Ibarguchi, J.I.G., 1997, Sequential development of the metamorphic aureole beneath the Ronda peridotites and its bearing on the tectonic evolution of the Betic Cordillera: Tectonophysics, v. 279, p. 227-252.